Stony Brook University

2D and 3D TEM Imaging on Nano-materials for Energy Application

A Thesis Presented

by

Jing Li

to

The Graduate School

in Partial Fulfillment of the

Requirements

for the Degree of

Master of Science

in

Material Science and Engineering

Stony Brook University

May 2014

Stony Brook University

The Graduate School

Jing Li

We, the thesis committee for the above candidate for the

Master of Science degree, hereby recommend

acceptance of this thesis.

Dong Su – Thesis Advisor
Staff Scientist, Center for Functional Nanomaterials at Brookhaven National Laboratory
and Adjunct Professor, Department of Material Science and Engineering

Alexander Orlov – Committee Member
Professor, Department of Material Science and Engineering

Huolin Xin– Committee Member
Staff Scientist, Center for Functional Nanomaterials at Brookhaven National Laboratory

This thesis is accepted by the Graduate School

Charles Taber
Dean of the Graduate School

Abstract

Nanostructured materials have attracted a growing attention as a novel solution of enlarging capacity and efficiency of energy storage devices. As a result, characterization of nanostructured materials is of paramount importance. Electron microanalysis renders a practical method to observe and analyze nanostructured materials. In this thesis, two dimensional and three dimensional electron microscopy characterizations have been used to investigate a suite of nanomaterials. The nanostructured materials studied in this thesis are core-shell structured FeNiPt nanorods(NRs), NiO nanosheets and DNA origami linked nanoassemblies.

I characterized the atomic-scale structures of shape-controlled ternary alloy nanocatalysts (Pt-Fe-Ni nanorods) using annular dark-field scanning transmission electron microscopy (ADF-STEM). The elemental distribution within the nanorods were obtained using spatially resolved electron energy loss spectroscopy (EELS). Our results suggested the Pt-Fe-Ni nanorods have a core-shell structure with Pt rich in the shell, and Fe/Ni rich in the core. This special core-shell structure can account for the superior catalytic activity of the nanorods for oxygen reduction reaction (ORR) reaction.

I investigated the lithiation processes of NiO nanosheets using in situ TEM. We observed two reaction modes. With real time tracking, I was able to quantify the propagation rate of the reaction front in both reaction modes. It was found the front propagation rate of the lateral reaction mode is approximately 100 times faster than that of the core-shell reaction. This work directly unravels the spatially dependent reaction pathways in lithium-ion battery electrodes.

To improve the throughput of electron tomography, I have established a model based tomographic method that only relies on the projected centroids of the nanoparticles and bypasses

the image intensity. This method only requires 5-10 tilt images and it is useful for calibrating a TEM goniometer and field/scan distortions. In this thesis, I will demonstrate this new method with the reconstruction of a DNA origami linked nanoassembly.

List of aberration

C_S	Spherical aberration
TEM	Transmission Electron Microscopy
SEM	Scanning Electron Microscopy
STEM	Scanning Transmission Electron Microscopy
EDS	X-ray Energy Dispersive Spectroscopy
EELS	Electron Energy Loss Spectroscopy
CCD	Charge-Coupled Device
HAADF	High Angle Annular Dark Field
BF	Bright field
DF	Dark Field
DP	Diffraction Pattern
CDF	Centered Dark Field
HR-TEM	High Resolution Transmission Electron Microscopy
SAD	Selected Area Diffraction
CBED	Convergent Beam Electron Diffraction
ORR	Oxygen Reduction Reaction
HOR	Hydrogen Oxidation Reaction
LUMO	Low Unoccupied Molecular Orbital
HOMO	High Occupied Molecular Orbital
SEI	Solid Electrolyte Interphase

NRs	Nanostructured Rods
NPs	Nanostructured Particle

List of figures

Acknowledgement

I would like to first express my sincere gratitude to my thesis advisor, Dr. Dong Su for his generous support, patience, immense knowledge and mentoring through my research and master thesis. I have enjoyed learning from him.

I want to give special thanks to Dr. Huolin Xin. His knowledge and experience has broaden my horizon. Part of my thesis is based on results simulated with his code. His guidance and advice made and continue to make my work possible.

I would like to thank my thesis committee members, Professor Alexander Orlov, for his time and his suggestions on my thesis.

This research was conducted in the Center for Functional Nanomaterials at Brookhaven National Laboratory supported by the U.S Department of Energy. I would like to thank the electron microscopy group for providing the help on operating TEM and characterizing and Dr. Eric Stach, Dr. Kai He, Dr. Lihua Zhang and Mr. Kim Kisslinger for their guidance.

I would like to thank the collaborators from Brown University, Prof. Shouheng Sun, Ms. Huiyuan Zhu for providing the samples of ternary alloy FeNiPt nanorods and AuMn nanoparticles. I want to also thank collaborators from Center for Functional Nanomaterials in Brookhaven national Laboratory, Dr. Oleg Gang and Mr. Ye Tian for providing the samples of DNA origami.

Last but not the least, I want to thank my parents for supporting me to pursue higher education and give me truly and sincerely love. And I also want to thank my best friend, Ruoqian Lin, for her accompany.

Table of Contents

Chapter 1 Prologue

1.1 Transmission Electron Microscopy

As time goes by, material scientists are no longer satisfied with materials they have known and the scale they have studied which, inevitable, lead the revolution of facilities. Nanotechnology has become more and more important in the past 20 years since people try to understand and control matter at dimensions of roughly 1 to 100 nanometers where various novel phenomena and structures can be achieved[1]. With the development of nanotechnology, transmission electron microscopy (TEM) plays an important role since it can retrieve the information of materials at atomic scale. TEM functions by a high-energy electron beam transmitted through a thin specimen while interacting with the specimen both elastically and inelastically, generating different kinds of signals, such as backscattered electrons, secondary electrons and X-ray. Information of morphology and crystal structure are given by TEM imaging and diffraction at atomic resolution while chemical composition and electronic states can be acquired by either X-ray Energy-Dispersive Spectroscopy (EDS) or Electron Energy-Loss Spectroscopy (EELS).This chapter will briefly introduce various TEM techniques to be used in this thesis.

1.1.1 Components of Transmission Electron Microscopy

TEM allows one to obtain real-space images and simultaneously diffraction information from specific region of interest in the specimen. As mentioned above, when electron beam transmitted through specimen, different interaction occurs and the information are retrieved by different detectors. To understand how the TEM function, it is necessary to understand the structure and the component of TEM. As shown in Figure *1*, a TEM primarily contains the electron source (gun), series of electromagnetic lens and electron detect systems. A high vacuum ($\mathbf{10^{-5}}$ to $\mathbf{10^{-9}}$

Pa) is required in high-voltage TEM to avoid generation of electrical arc at the cathode of gun. Since the TEM specimen needs to be inserted and extracted rapidly, multiple pumping vacuum system and airlock are essential especially for high-voltage TEMs. In addition, the computer control system is crucial to operate the TEM as well as to detect signals and process data.

For different types of TEM there are different kind of electron gun. One is thermionic emission gun which emit electrons when heated, and the other is field emission gun which produces electrons when an intense electric field is applied to it. Materials with low "work function" (Φ), like LaB_6, are perfect as thermionic source. This can be explained by Richardson's Law [2] (Equation 1-1) where J is current density from the source, T for operating temperature in Kelvin, k as Boltzmann's constant and A is Richardson's constant based on source material:

$$\boldsymbol{J = AT^2 e^{\frac{-\Phi}{kT}}} \tag{1-1}$$

The principle of field emission gun, which is different from thermionic emission gun, is the electric field (E) is impressively increased at the sharp point. From equation 1-2, it is obvious that materials with sharper tip can achieve higher electric field. One of the best option is Tungsten wire which can be easily produced with a tip radius < 0.1μm [3].

$$\boldsymbol{E = \frac{V}{r}} \tag{1-2}$$

Lens system is important in TEM since they decide the quality of the electronic optical system and functionize by changing current. There are several lenses in a TEM and Figure *1* (B) indicates primary lenses and the route of electron beam.In a particular lens, beam converge at different plane forms differently, like beam focus on back focal plane Throught changing the

current of the lens, one can obtain TEM image or diffraction pattern as well as changing magnification and focus.

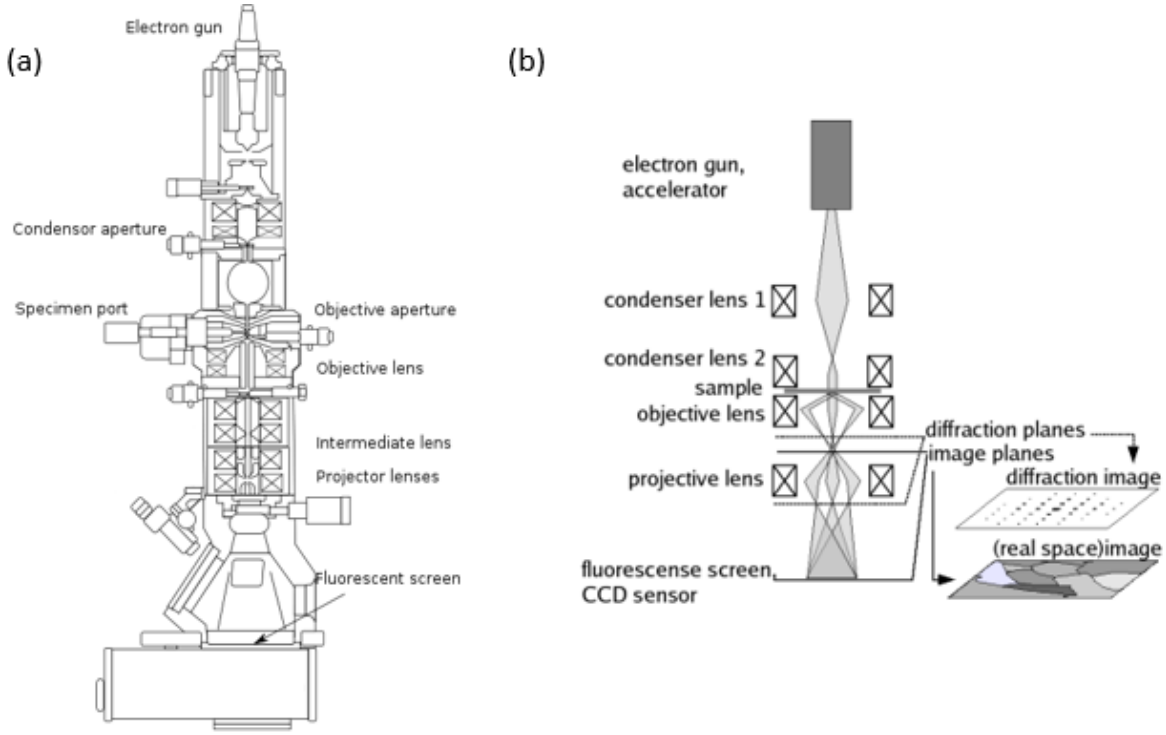

Figure 1(a) Schematic diagram of Transmission Electron Microscope and (b) Ray diagram of transmission electron microscope. （Figure 1 adapted from Wikipedia）

1.1.2 Transmission Electron Microscopy Techniques

TEM encompasses many different techniques such as HRTEM, Scanning Transmission Electron Microscopy (STEM), Diffraction Pattern (DP), electron holography, EELS, EDX and Tomography. Each technique offers different aspects to characterize the material. Since DP gives the information of phase from selected regions, images formed by selected diffraction spots can show diffraction contrast, which relates to the crystal orientation and phase[4]. STEM, is working in scanning mode with the focus electron probe, it combines the advantages of both Scanning Electron Microscopy (SEM) and TEM. And its High-Angle Annular Dark Field (HAADF)

imaging technique which can provide atomic number (Z) contrast images[5]. Spectroscopy techniques such as EELS and EDS are perfect for identifying the composition and the electronic state at very local area[6]. Tomography acquires images within large range of tilting angle (-70° to +70°) followed with tomographic reconstruction[7], we can obtain morphology information of specimen in three dimension.

1.1.2.1 Imaging: TEM and STEM

1.1.2.1.1 Diffraction Contrast TEM

Since thin film crystalline specimen usually has uniformed thickness and almost same atomic number, mass-thickness contrast cannot ensure perfect contrast[8] so that diffraction contrast come into view. Different from incoherent elastic electron scattering lead to mass-thickness contrast, coherent elastic scattering generates diffraction contrast image. To achieve ideal strong diffraction contrast, we must meet two-beam condition[9] which only has one strong diffracted beam except from direct beam. Using an aperture of objective lens to blocks diffraction beam can help to obtain Bright Field (BF) image, otherwise, get Dark Field (DF) image. However, the beam we use here is off-axis beam which can cause severe optical aberration[10]. Therefore, another method is wildly used for forming DF images. First, say there is a bright spot hkl, we usually tilt the incident beam through 2θ to locate $\bar{\boldsymbol{h}}\bar{\boldsymbol{k}}\bar{\boldsymbol{l}}$ which used to be weak pass through aperture (ray diagram shows in Figure *2*) and this kind of image called Centered Dark Field (CDF) image which has much better contrast than BF and widely used in study of metallic thin film.

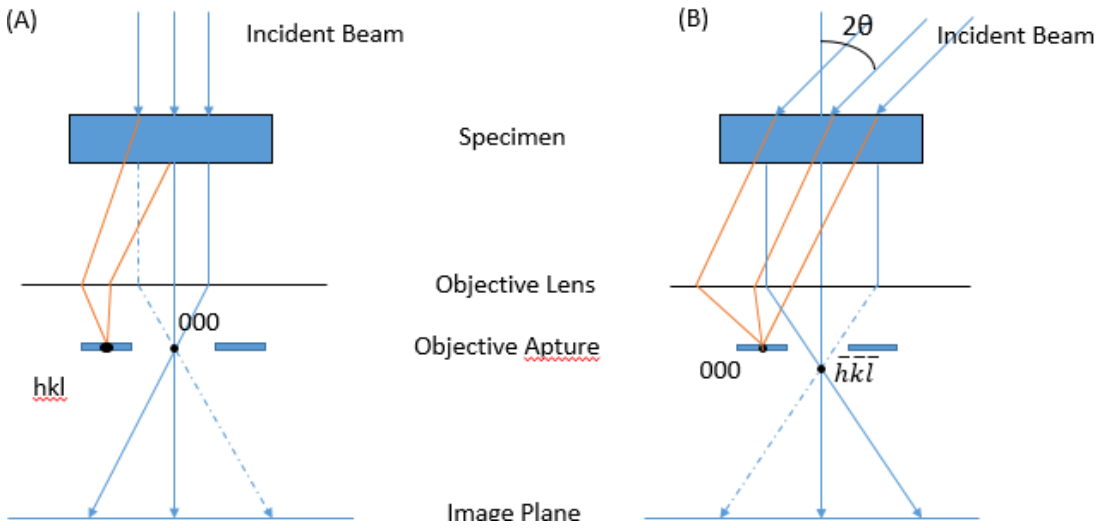

Figure 2 Standard two-beam condition involve 000 spot and hkl spot bright (A) to form BF image, let transmission beam pass through. (B) To form CDF, tilt incident beam through 2θ located $\bar{h}\bar{k}\bar{l}$ on the axis.

1.1.2.1.2 High-resolution TEM

Generally speaking, high-resolution TEM (HRTEM) is imaging which lattice information are observed or atomic resolution is achieved. Different from diffraction contrast TEM, HRTEM images are formed by multiple diffraction beam which compared with diffraction contrast imaging is known as phase contrast imaging[11]. Nowadays, the highest point resolution achieved in phase contrast TEM is around 0.005nm[12]. Therefore, single atom and its defects and nanostructure can be resolved by HRTEM.

However, phase-contrast imaging is susceptible to aberration of lenses in microscope, such as spherical aberration (C_S). Furthermore, the contrast is decided by interference in imaging plane (usually a digital pixel detector like CCD camera) with electron wave itself. As the results of interaction with specimen, the electron exit wave below specimen works as a function of spatial frequency. And high spatial frequency is simply corresponded with large distance in reciprocal

space which determined by the distance between back focal plane and image plane). Thus, it is easier to obtain HRTEM through defocus and astigmatism.

1.1.2.1.3 STEM

Figure *3* [13] shows main component of an aberration corrected STEM. Electron beam emitted from a source and focus to a small probe passing through sets of lenses and then transmitted through the specimen. Detectors around sample are used to collect elastic or inelastic electrons to form different types of images while scanning coil works on electron beam as it was in SEM.

STEM imaging is extraordinary by its Z-contrast imaging which offered by a high-angle annular dark field (HAADF) detector. These images provide good compositional contrast especially where sample and support material have huge difference in atomic number. Furthermore, since the small probe of electron beam STEM can accurately control region of interest and greatly improve the spatial resolution of EELS and EDS.

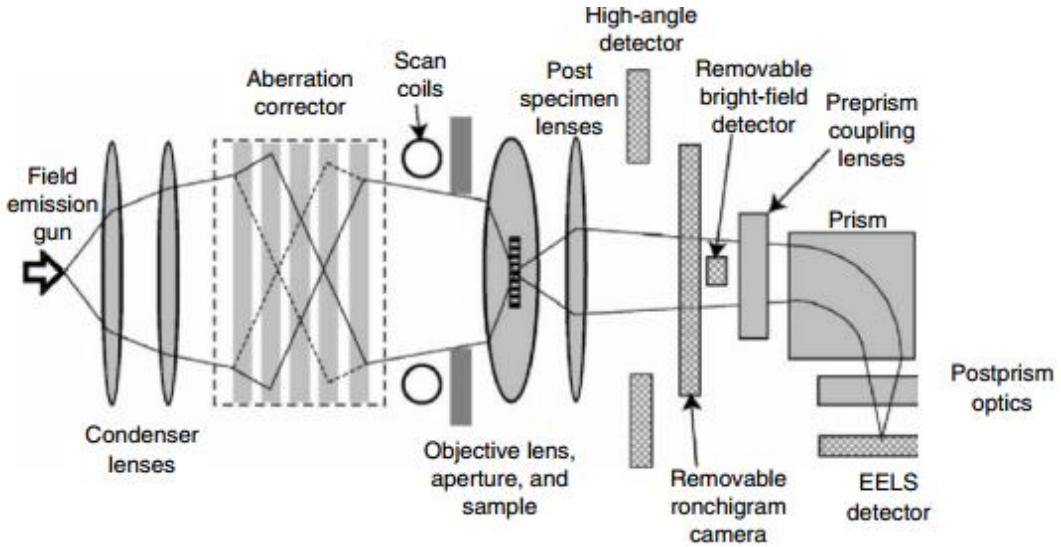

Figure 3 Schematic diagram of main components of high-resolution dedicated STEM. Figure adapted from ref. 13

1.1.2.2 Diffraction

Different from imaging, diffraction patterns are formed when electron beam focus on back focal plane which shows crystalline structure and phase information from region of interest. Generally, there are two types of DPs usually used: one is Selected-area Diffraction (SAD) and the other is Convergent-beam Electron Diffraction (CBED), as Figure *4*[14] shows. An SAD is formed under broad and parallel electron beam with a selected-area aperture at image plane of objective lens to select the diffracted region of the specimen[15]. As all DPs, SAD patterns are formed in reciprocal space where lattice information are reflect as diffraction spots. To accurately analyze crystalline information, tilting crystalline material into low-index zone axes is essential[16]. Moreover, SAD often shows as ring pattern for nanomaterial since it contains various orientation in small volume.

For CBED, the beam is convergent and relatively small (usually 10-100nm in diameter)[17] rather than broad and parallel beam in SAD. Compared to SAD, CBED formed by much smaller area which enables precisely localized analysis. Furthermore, CBED consist information of discs rather than spots which can reveal more details and exploit more aspects of specimen's microstructure[18, 19]. And a new technique which combine STEM with CBED can record CBED patterns for each pixel during the electron beam scanning form every single scan and offers broader information of crystal symmetry and elemental distribution[20].

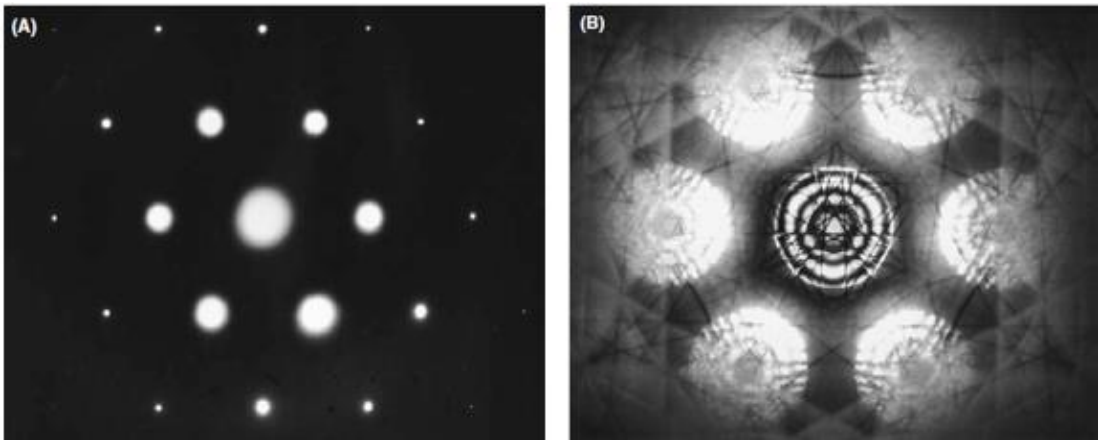

Figure 4(A) SAD patterns from [111] Si and (B) CBED pattern from [111] Si showing dynamic contrast. (Figures adapted from ref.14)

1.1.2.3 Spectroscopy: EELS and EDS

Ionizing radiation which means tightly bound inner-shell electrons are removed from the attractive field of nucleus often happens when high energy beam irradiate on specimen[21]. Signals emitted by ionizing radiation all benefits for chemical analysis especially EELS and EDS (Figure *5*).

Inelastic scattering is primarily an electron-electron interaction which, of course, result in energy loss and change of momentum. Low energy loss which means energy-loss electrons in less than 50 eV, generally occurred by interaction with Plasmon oscillations[22]. The energy E_p lost by beam electron when it generates a plasmon of frequency ω_p is given by:

$$\boldsymbol{E_p = \frac{h}{2\pi}\omega_p = \frac{h}{2\pi}\left(\frac{ne^2}{\varepsilon_0 m}\right)^{\frac{1}{2}}} \qquad (1\text{-}3)$$

Where h is Planck's constant, e and m are the electron charge and effective mass, $\boldsymbol{\varepsilon_0}$ is the permittivity of free path, and n is the free-electron density[23]. Form function 1-3, we can conclude that plasmon loss dominates in materials with free electrons. And at higher energy loss, the

spectrum contains information from inelastic interactions with the inner or core shell. Inner-shell ionization can produce intensity edges in spectrum which is atomically characteristic, thus always used for elemental analysis[24]. As mentioned before, the high energy beam can eject electrons from inner-shell ionization which lead to vacancies. After that vacancies are filled by electrons from higher energy shells and electron energy lost with the transitions are emitted as X-ray. Therefore, the X-ray can represent for atomic species and the EDS is allowed to identify chemical composition of specimen.

Both EDS and EELS are caused by inner-shell ionization but different in some aspects[25]. Compared to EDS, EELS has better collection efficiency so that can save time in acquiring spectrum which decrease damage form incident beam. Moreover, EELS is much more chemical sensitive than EDS, in other words, EELS can offer better identification of elements with small atomic number. And because of the ionization edge, EELS can analyze atomic bonding state or valence of elements which provide more detailed information about the specimen.

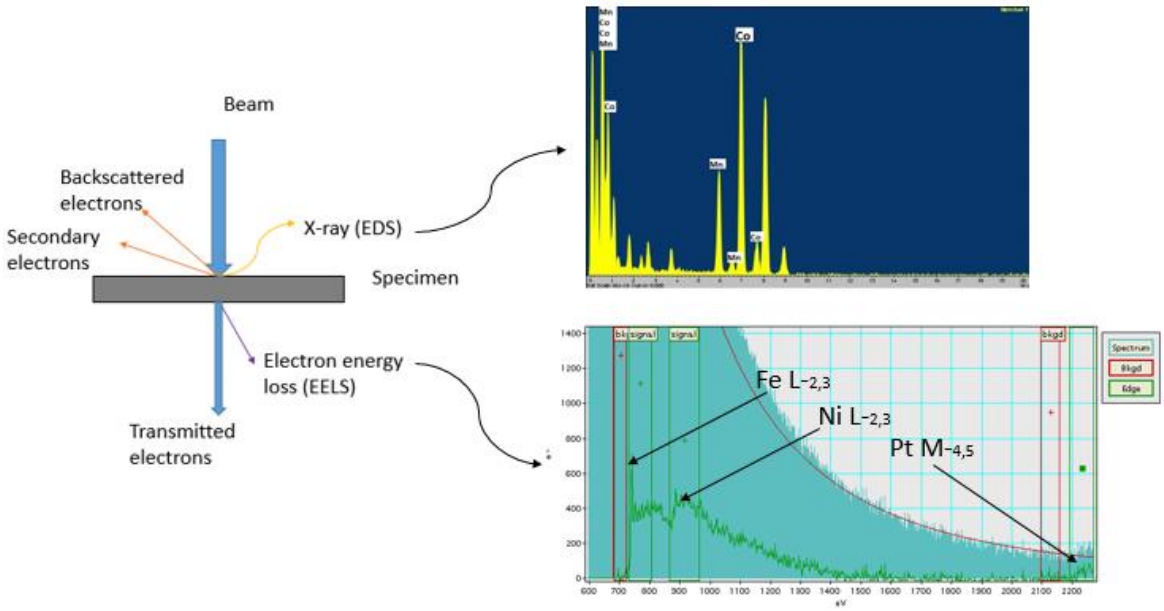

Figure 5 Schematic diagram of interaction between incident beam and specimen which generate signals: a) EDS formed by emitted X-ray and b) EELS obtained when fast electrons lost their energy

1.1.2.4 Tomography

Tomography is a growing technique for investigating shape, size, distribution, and elemental information of materials in all three dimensions (3-D). With the development of this technique, tomography is now capable to routinely achieve one nanometer resolution, and to determine the elemental distribution of materials in 3-D[26].

To do tomography, first is to acquire images from a wide angular range (-70° to +70°). After data acquisition, tomograms can reconstructed by the filtered back-projection method[27]Figure *6* gives a pictorial view of how tomography works. From the tomographic reconstructions, we can achieve three-dimensional analysis of sample shapes and morphology. To obtain directly interpretable results, coherent phase and diffraction contrast needed to be suppressed. ADF-STEM imaging is preferred for materials tomography. Since the the sample need to be tilted to high angular ranges, the specimen holder be thin and narrow to fit into the limited space between the pole pieces.

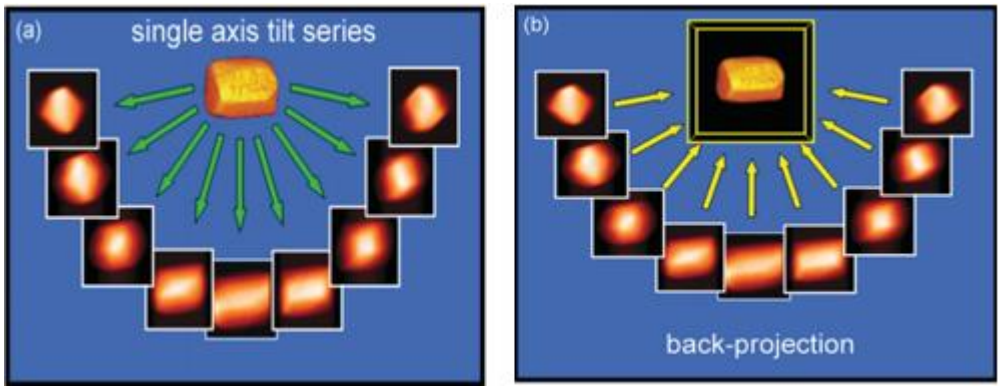

Figure 6 Schematic diagram of tomographic reconstruction by back-projection method. a) A series of images are required by tilting specimen, and these images are back projected in b) along with their original tilt directions into a three-dimensional object space. Figure adapted from ref. 27

1.2 Nanocatalyst

1.2.1 Introduction of Nanocatalysts

The general purpose of catalysts is to increase the speed of a given reaction. It can be achieved by kinetic ways which will not impact on thermodynamic properties directly of the chemical system[28]. As it is known, there are three ways to accelerate a chemical reaction though catalyst: lower the activation energy for the reaction, as a promoter to bond the reactant more tightly which improve the reaction efficiency, or build a higher barrier of one species when it habit the other two or more products from generating. But the key issue defines the efficiency of a catalyst is the ratio of surface area and volume. And it is known to all that high ratio of surface area to volume is much favorable for chemical reaction.

Therefore, catalysts in smaller size maintain higher surface to volume ratio which ensure higher activity, in other words, nanocatalysts are prior in catalytic activity than traditional catalysts.

Nanocatalysts are defined as the catalysts have at least one dimension is smaller than 100 nm, including nanolayers (only one dimension at nanoscale), nanowires and nanotube, and nanoparticles. Nanocatalysts have much greater catalytic activity not only because they have extremely small size which limits the surface to volume ratio but also when materials made at nanoscale they will achieve properties which cannot be found at their macroscopic counterparts[29].

1.2.2 Application of nanocatalysts

Unprecedented properties are achieved using nanocatalysts. Among all applications, there are tremendous interests in the preparation of electro-catalysts for fuel cell in recent decades[30].

A device that can convert chemical energy form a fuel into electricity through a chemical reaction, such as Oxygen Reduction Reaction (ORR), is called fuel cell. To generate electricity, water, heat and minority of nitrogen dioxide and other emissions are unavoidable since hydrogen is the most common fuel in fuel cell. Generally speaking, the efficiency of fuel cell is between 40%-60% [31] but through nanocatalysts it will improved.

Investigation of Oh [32] showed that Pt is perfect catalyst for fuel cell. But Pt is too expensive and when for ORR reaction, Pt will be poisoned by CO gas which reduce the catalytic efficiency. To reduce the costs of the nanocatalysts, Pt alloyed with other metal M, M is like Fe, Co or Ni and a Pt-shell with M-core nanoparticles are synthesized to achieve high catalytic activity with increased catalyst stability especially when Pt is in a one-dimensional (1D) nanostructure[33]. However, for the hydrogen oxidation reaction (HOR) impurities as carbon monoxide (CO) can severely deactivate Pt catalysts which, in other words, decrease the efficiency. To overcome this shortage, Yu-chi Hsieh [34] find out that the single crystalline Ru cores with well-defined Pt bilayer shells can alleviate the deactivating effect of CO and opens a door for using inexpensive reformates as the fuel as well.

1.3 Electrode materials for Lithium-ion Battery

1.3.1 Introduction of Lithium-ion Battery

Lithium-ion battery(LIB) is a kind of the rechargeable battery in which lithium ions move from cathode to anode during discharge and it also important for its high stored volume and gravimetric energy density. The main components of lithium-ion battery are electrode (contains cathode and anode) and electrolyte (Figure *7*a). For comersialized LIB, anode is made from carbon while cathode is metal oxide. Figure *7*b[35] shows relative electron energies in a

thermodynamic stable battery with an aqueous electrolyte. As the diagram indicates, there are three ways to improve the capacity of lithium-ion battery: the first one is to broad the "window" of electrolyte which means bigger energy separation E_g between lowest unoccupied molecular orbital (LUMO) and highest occupied molecular orbital (HOMO) of electrolyte; second one is finding appropriate electrode material that can match the "window" of electrolyte as well as be chemical stable in the electrolyte; and the last is to form a passivating SEI layer. A passivating SEI layer will be formed when electrochemical potential of cathode and anode are outside the "window" of electrolyte. As a stable SEI layer, it must can be self-healed when battery is about to broken since electrode volume change in charge and discharge cycles. How to form a SEI layer which is benefit for lithium-ion battery, is still an open question.

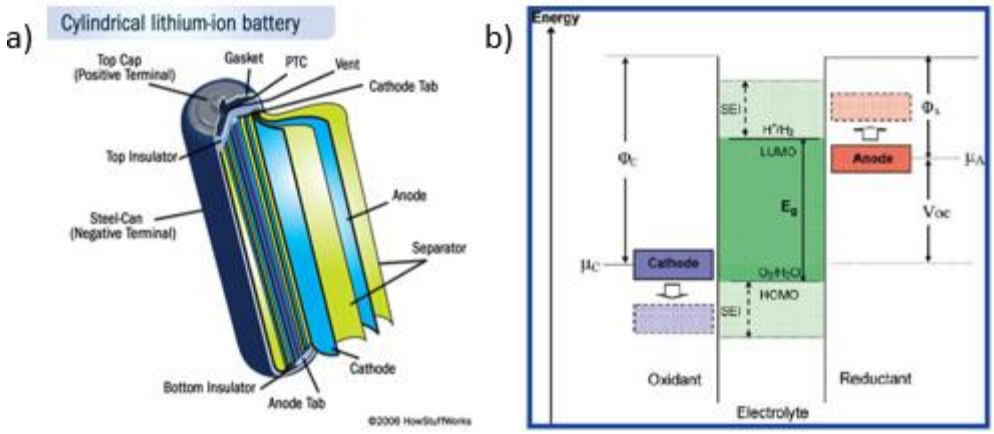

Figure 7 Schematic diagrams illustrate (a) structure of cylindrical lithium-ion battery and (b) electron energy of battery with aqueous electrolyte: Φ_A and Φ_C are work function for anode and cathode; when electrochemical potentials μ_A and μ_C are beyond the "window", a kinetic driven SEI layer will be formed. (Figures adapted from ref. 36)

1.3.2 Electrode materials for lithium-ion battery

Ideal electrode materials must have μ_A and μ_C matching LUMO and HOMO of lithium-ion electrolyte. Factors that can determine the electrochemical potential of cathode and anode are not only their Fermi energy but also the energy of a redox couple of a transition-metal cation[36]. The

energy of a redox couple depends on formal valence state of cation, covalent component of its nearest neighbor bonding which influenced by the structure and the intrinsic voltage limit. Despite of limitation mentioned above, the slow solid-state diffusion of lithium-ion within the electrode material limits the rate capabilities of lithium-ion battery. And nanostructured electrode materials solved this problem since the distance Li^+ need to diffuse is restricted to the radius of nanoparticle which is much shorter than conventional materials. As Charles R. Sides[36] noticed the nanofiber Sn-based anode derived from oxygen of tin (e.g., SnO_2) has improved the rate of capabilities (Figure *8*a). At highest C rate, the capacity that nanostructured electrode delivered was more than two orders of magnitude higher than conventional electrodes. In additional, nanostructured transition-oxides as negative-electrode materials provided high electrochemical capacities and capacity retention[37]. As they observed, the mechanism of reaction between lithium and these metal oxides, such as NiO, was different from conventional ones. Since these nano-sized transit metallic oxides crystalline into a rock-salt structure which reduced available empty sites for Li ions. Furthermore, the chemical and physical phenomena are strongly affected when dealing with nano-sized materials. Therefore, electrochemically driven size confinement of metal particles are believed to enhance electrochemical reactivity and capacity retention (Figure *8*b).

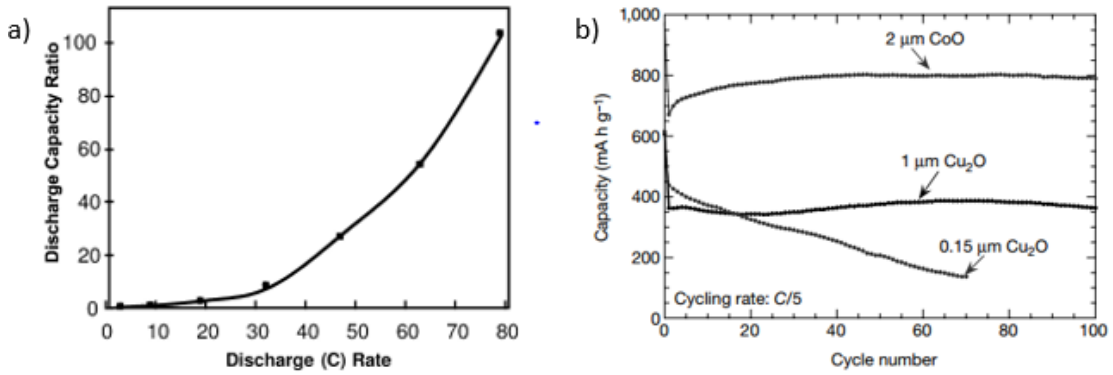

Figure 8 (a) Discharge capability ration versus discharge rate of Sn-based nanostructured electrode as compared with thin-film controlled electrode. (b)Capacity fading of Cu_2O-based electrode as a function of particle size (figures adapted from ref.36 and ref.37)

Chapter 2 Experimental

2.1 Nanocatalysts

FePtNi nanorods (NRs) were synthesized by our collaborator at Brown University using the thermal decomposition of iron pentacarbonyl [$Fe(CO)_5$] and the reduction of metal acetylacetonates [$Pt(acac)_2$ and $Ni(acac)_2$][38]. At 160°C, a mixture of $Ni(acac)_2$ and oleylamine (OAm) was added into the solution to control the stabilization and the growth of NRs. In the synthesis, one dimensional (1D) FePt NRs were formed before Ni precursor was added which indicated that FePt NRs were served as template and Ni can be incorporated into NRs by intermetallic diffusion. The key factor to form ternary NRs is pentacarbonyl which avoid presence of irregular NiPt NPs. When Fe/Pt precursor ratio was increased to 2:1, the Fe/Pt ratio remained at 1:1, Ni salt was mainly reduced by $Fe(CO)_5$ and under consequent high temperature (240°C) aging, ternary 1D FePtNi NRs were formed through atomic diffusion.

The phase-contrast TEM images were taken with a JOEL 2100F TEM operating at 200 keV, equipped with Gatan image filter system. The spatial resolution is about 0.17nm at TEM mode. STEM measurements including HAADF-STEM images and EELS were performed through Hitachi HD 2700C at 200 keV which is equipped with a cold-field emission electron source and a CEOS probe aberration corrector. The sample for both TEM and STEM was prepared by drop casting the ethanolic suspension of carbon-supported NRs on carbon-coated copper grid (lacey carbon support film, 300 mesh,Ted Pella Inc.) and loaded on JEOL double tilt low background Be holder (*Figure 9*a) and FIB/STEM compatible specimen holder (*Figure 9*b).

Elemental line-scans and 2D mappings were made with high-resolution EELS detector (Gatan Enfina-ER). The exposure time for each spot was about 0.07s for EELS line-scan and 0.05s for

2D mapping. Extracting the Fe, Ni and Pt EElS signals from the EELS spectrum which had been wiped off background reference (scripts written by Huolin Xin et al.) and an integration window at each elements characterized edges.

2.2 Electrode material for lithium-ion battery

A sample loaded onto cooper half-grids with amorphous carbon thin film was developed and used for studying the electrochemical reaction of NiO nanosheet. A thin layer of lithium metal was coated on a sharp tungsten tip. And assembled them in a glove box then transfer into the TEM column with Ar-filled bag. 200keV field-emission S/TEM (JOEL 2100F) equipped with a Gatan image filter spectrometer was used for obtaining images and DPs with nanofactory Instrument AB (Figure 9c). ADF-STEM images were recorded in scanning TEM mode for local analysis. And high-resolution ADF-STEM images and spectra were acquired from the lithiated samples in Hitachi 2700D with a probe aberration-correction system to identify crystallographic orientation and phase conversion after lithiation.

2.3 Nanoscale assemblies

Tomograms were required through JOEL JEM 2100 TEM operating at 200 keV, equipped with thermionic emission electron source. Tilt series images were recorded form -60° to +60° with 2° intervals. The sample for electron cryo-microscopy was purified at a concentration of ~10 nM in 10 mM Tris buffer (pH 7.6) ith 20 mM $MgCl_2$, 5mM NaCl and 1mM EDTA. And before preparing the grids to resolve multimers formed by blunt-end stacking, purified sample was heated in a water bath at 37°C for 1 hour. Aliquots of 5μL were incubated for 5 minutes on glow-discharged holey carbon grids with an ultrathin carbon film on top, blotted, and plunge-frozen in liquid ethane. Specimen loaded on the Fischione advanced tomographic(Figure 9d) titling form -

60° to +60° with 2° intervals in which tilt series were required. The reconstruction of tomograms was done by the e^{-} Tomo software suite written by Robert Hovden et al. and visualized by Avizo 6.3.

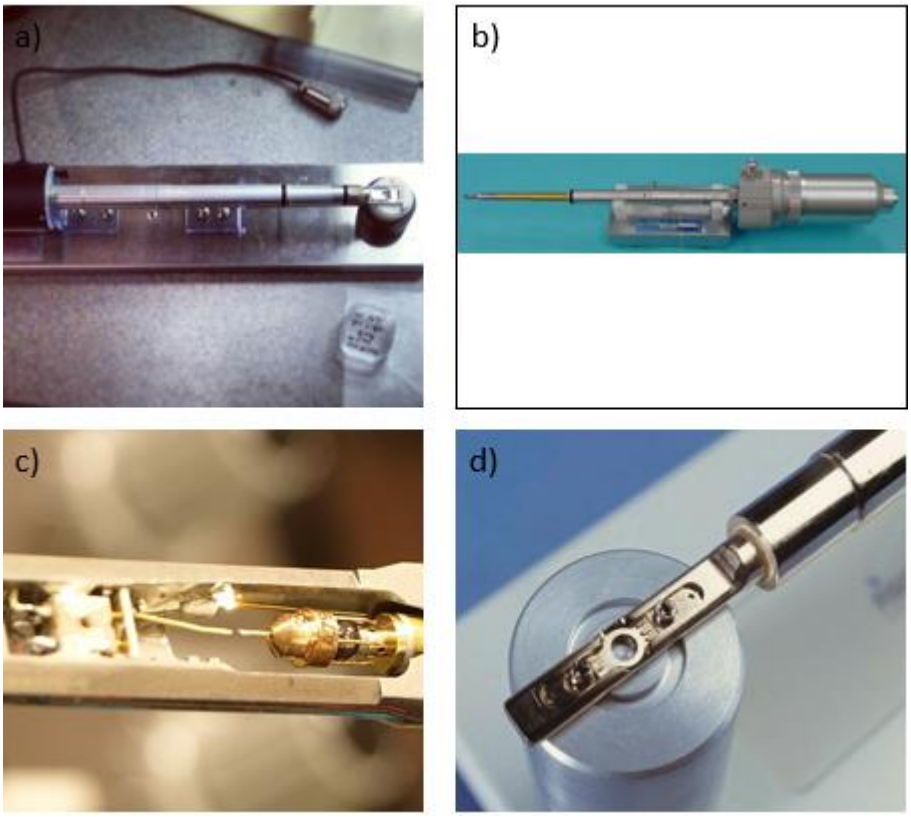

Figure 9 (a) JEOL double tilt low background Be holder (b) Schematic diagram illustrate in-situ TEM electrochemical test (c) Nanofabrication single tilt holder (d) Fischione advanced tomographic holder

Chapter 3 Results and Discussion

3.1 Characterization of Nanocatalysts

The FePtNi NRs synthesized as mentioned before are structurally well-defined. As shown in Figure *10*, two-headed NRs are averagely 26nm long and the widest part is about 5 nm. From the high resolution STEM image of figure 9d, we observe the lattice arrangement between surface and center is different which infer different crystalline structure. Furthermore, in Figure *10*e,

there are discrepant brightness between surface and center in <110> direction, which indicates there are chemical inhomogeneity between core and shell. However, simply characterizing STEM images is still insufficient to declare the core-shell structure, hence, we need STEM EELS line-scan to ensure the chemical composition as well as the distribution.

As mentioned above, EELS is the spectroscopy that contains information from inelastic interactions with inner shell electrons as well as valence electrons, and the intensity at edges depends on the empty density of state (DOS) of particular atoms. Figure *11* (a), (b) and (d) indicate how line-scan works in order: trajectory that electron beam pass through the specimen was labeled as the red arrow in Figure *11*a; with the inelastic interaction, we can obtain spectrum (as shown in Figure *11*b) of extracted intensity edges (Figure *11*d), the existence of Iron (L-edges 721eV), Nickel (L-edges 872eV) and Platinum (M-edges 2202eV) are confirmed. Analyzing EELS signals of each element with uniform maximum value, compositional distribution is acquired as Figure *11*c. From this line scan, it is obvious to prove that Nickel and Iron mainly locate in the center of nanorod while Platinum is on the surface. To visualize the 2D distribution of the elements, one can do 2D mapping on this particles. However, since 2D mapping requires more collection time and a more severe beam-damage would destroy the nanoparticles before one can obtain any meaningful information. The attempt to map distribution of Fe-Ni-Pt has been failed. Therefore, we choose another specimen, AuMn nanoparticles (NPs), which directly laid on carbon black to illustrate the benefit of 2D mapping.

2D elemental mapping was obtained by scanning the electron beam over an area of interest. Simultaneous ADF signal and EELS signal can be obtained by ADF detector and Enfina spectrometer respectively. Spatial resolution is determined by beam size. Using a similar procedure of 1D line scan (Figure *11*a). The final elemental distribution can be obtained. The

Au/Mn NPs were directly loaded on grid and air-annealed at 170°C to form Au/MnO composition. When manganese rich alloy ($Au_{44}Mn_{36}$) were air-annealed, core-shell structured Au/MnO was develop. This core-shell structure was confirmed by HAADF-STEM 2D mapping. 2D elemental mapping at 48 × 48 pixels were recorded with an energy dispersion of 0.5eV/ch and a 1.3Å electron probe at about 70 pA through a Hitachi-STEM operated at 200 keV. After analysis and characterization, I obtained an overlay image (Figure *12*b) of gold and manganese shows good coincidence about atomic position, the core-shell structure with manganese-rich outer shell is resolved.

Through techniques mentioned above, we can declare that the FeNiPt NRs are core-shell structure with well-controlled shape, moreover, Fe and Ni distribute in the core while Pt in the shell. For materials insusceptible for beam damage, 2D mapping is more preferable to obtain composition distribution.

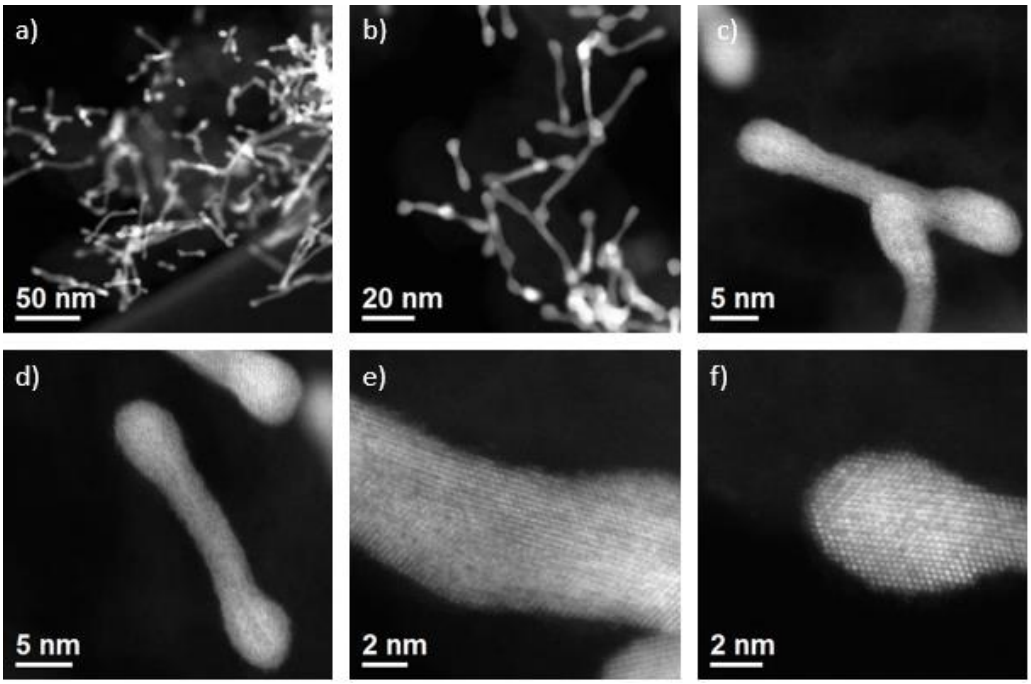

Figure 10 Morphology of structurally well-defined FeNiPt core-shell NRs at magnification of (a)400K (b) 800K (c) 3000K (d) 3500K (e) 7000K and (f) 8000K

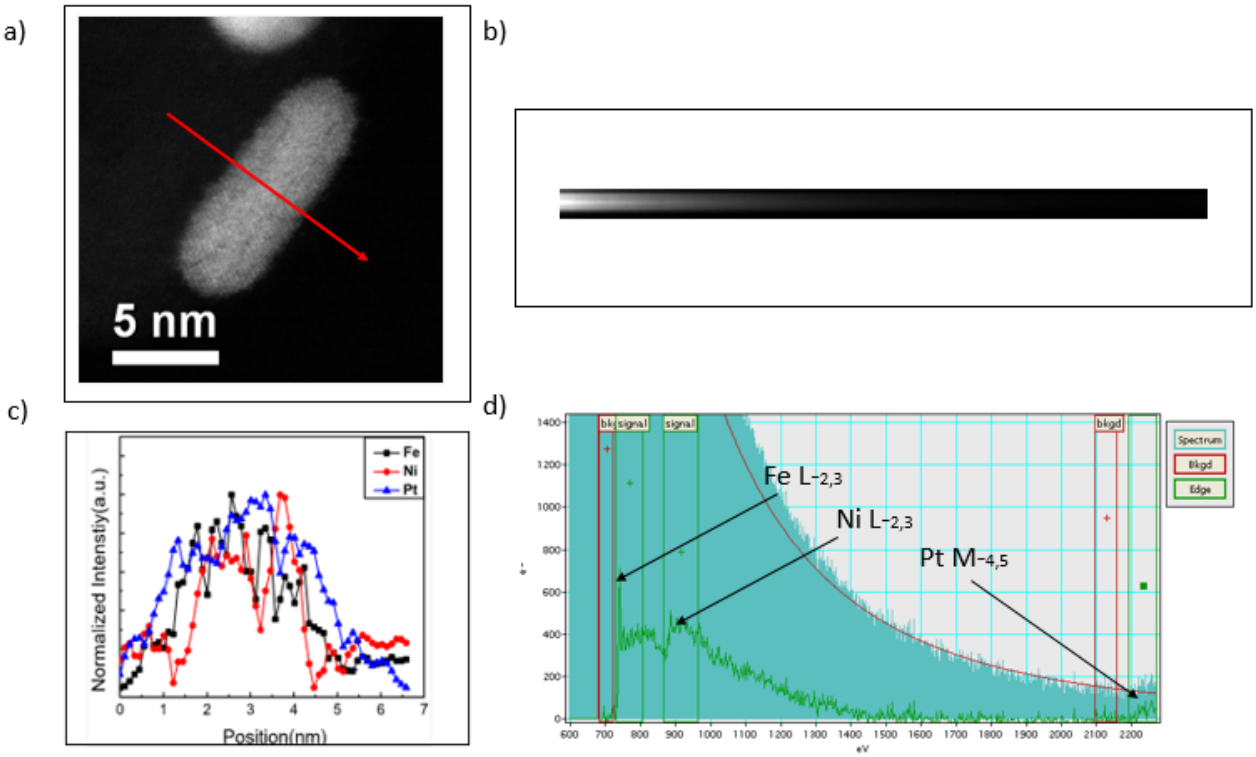

Figure 11 General procedures for EELS analysis: (a) line-scan across the specimen in the direction as red arrow shows. (b) Electron energy loss spectrum obtained after scanning. (c)Extracted Iron, nickel and platinum concentration along the arrow profile in (a). (d) Signals extracted (b) which indicates the existence of different elements by their characterized edges

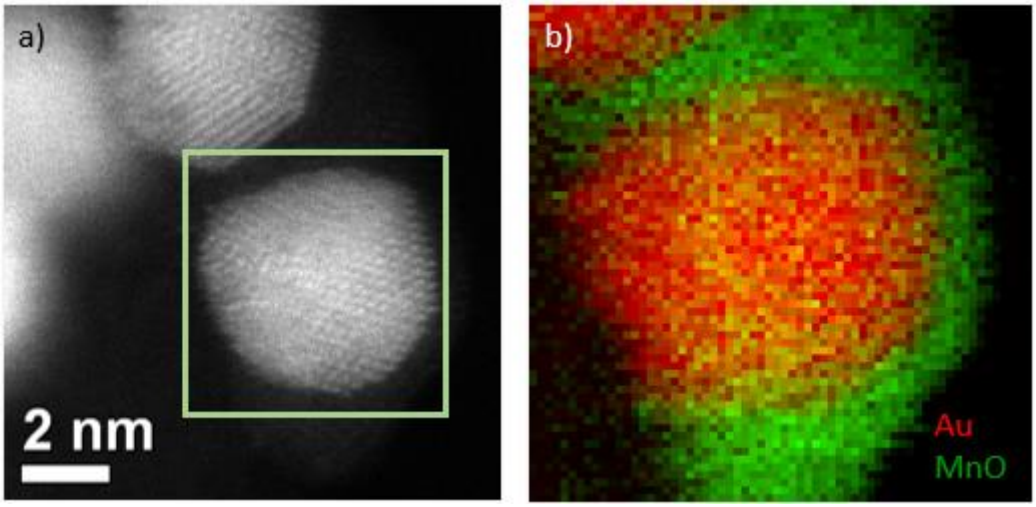

Figure 12 2D elemental mapping of Au/Mn core-shell structure NPs: (a) area of interest where beam scans pixel by pixel (b) Overlay 2D mapping of Au and MnO

3.2 Characterization of Electrode materials for Lithium-ion Battery

Under the condition mentioned in experimental part, real time tracking of lithiation reaction on NiO nanosheet was recorded. During lithiation, we observed different types of reaction modes: Lateral (Figure *13*a-c), core-shell (Figure *13*d-f) and surface heterogeneous reaction happened at the same time. All reactions exhibit discernible nickel nanoparticles nucleated on the NiO matrix during cycling and propagated into vicinity until the fronts met.

After nucleation, nickel nanoparticles propagated through diffusion. As we all know, the lower packing density the higher migration ratio, moreover, activation energy of surface is half of bulk which means the diffusion coefficient of bulk diffusion (D_B) is smaller than diffusion coefficient of surface diffusion (D_L). In addition, a particle nucleation/propagation process of electrochemical driven phase conversion is generally taken as homogeneous phase conversion. However, with the existence of planer defects, it can be spontaneously replaced by heterogeneous reaction which is direction-preferred.

For NiO framework, the top surfaces are primarily (111) facets. And from observation, we noticed that lateral reaction is about 100 times faster than the slowest core-shell reaction, though both lateral reaction and core-shell reaction are bulk diffusion. We still don't understand the orgins of the difference. We are working on solving this problem through our collaboration with theoriests at MIT. Above all, we can generally conclude that the lithiation process of lithium-ion battery is spatial direction dependent.

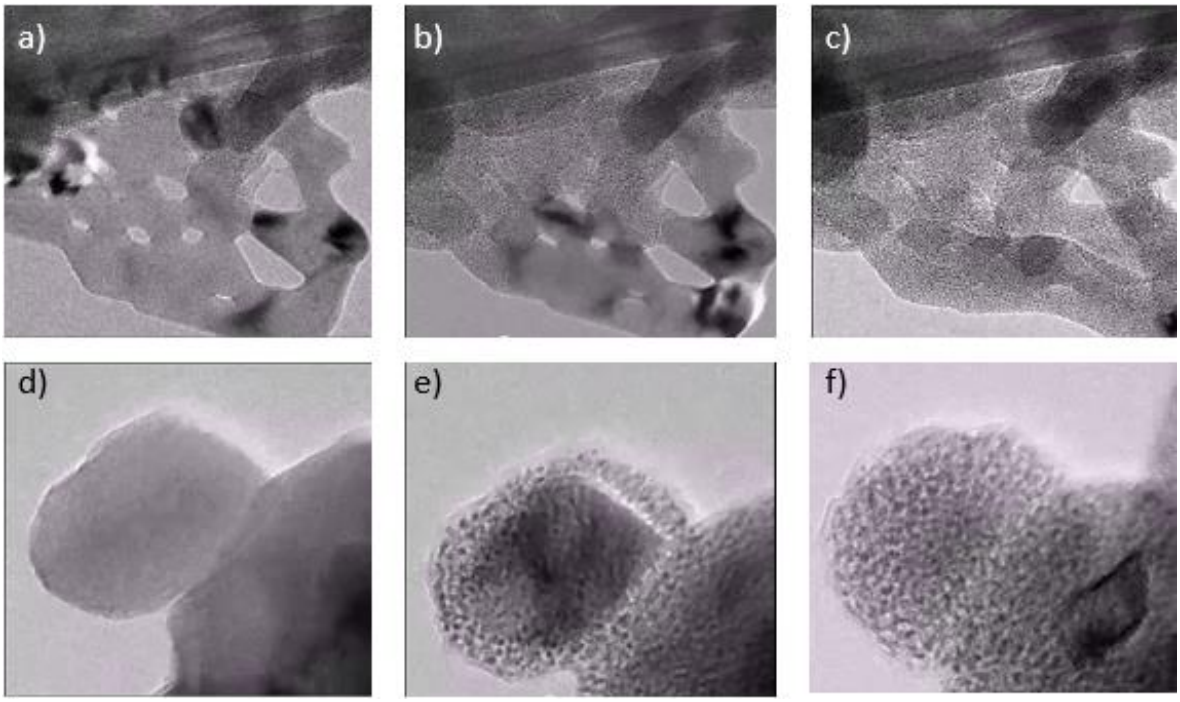

Figure 13 Time sequence TEM images of NiO-lithiation. (a-c) Lateral reaction: (a) Pristine NiO nanosheet. (b) NiO nanosheet with a 50% SOC (discharging 30 seconds) (c) NiO nanosheet with a fully discharged state (65 seconds). (d-f) core-shell reaction: (d) Pristine NiO nanosheet (e) NiO nanosheet with a 50% SOC (discharging 1500 seconds) (f) NiO nanosheet with a fully discharge state (3600 seconds).

3.3 Electron Tomography for Nanoscale Assemblies

When periodic lattices are break into clusters, small angle X-ray scattering is not conclusive because of the inhomogeneity of the nano clusters. Therefore, electron tomography is desirable to reconstruct the three dimensional structure. However, it generally takes 40 minutes or 2-4 hours to record a tilt series (70-140 images) of BF-TEM or ADF-STEM respectively. According to the model we built, it only needs, in principle, three tilt images to solve all unknown variables.

This method is based on measuring the geometric centers $(\mathbf{x^i(\theta)}, \mathbf{y^i(\theta)})$ of nanoparticles in the projected images as a function of the tilt angle $\boldsymbol{\theta}$, where the superscript i is the label for each individual particle. The frame of reference/rotation axis can be shifted to a specific particle n by a pre-subtraction procedure, i.e., $\left(\mathbf{x^i(\theta)}, \mathbf{y^i(\theta)}\right) = \left(\mathbf{x^i(\theta)}, \mathbf{y^i(\theta)}\right) - \left(\mathbf{x^n(\theta)}, \mathbf{y^n(\theta)}\right)$. The three-

dimensional (3-D) positions of the particles at zero degree tilt in the particle n reference frame can be retrieved by a nonlinear least squares fitting of the below equation (3-1):

$$\begin{pmatrix} x^i(\theta) \\ y^i(\theta) \\ z^i(\theta) \end{pmatrix} = \begin{pmatrix} \cos\alpha & -\sin\alpha & 0 \\ \sin\alpha & \cos\alpha & 0 \\ 0 & 0 & 1 \end{pmatrix} \begin{pmatrix} \cos\beta & 0 & \sin\beta \\ 0 & 1 & 0 \\ -\sin\beta & 0 & \cos\beta \end{pmatrix} \begin{pmatrix} 1 & 0 & 0 \\ 0 & \cos\theta & -\sin\theta \\ 0 & \sin\theta & \cos\theta \end{pmatrix} \begin{pmatrix} x_0^i \\ y_0^i \\ z_0^i \end{pmatrix} \qquad (3\text{-}1)$$

where, $\boldsymbol{\alpha}$ is the image/scan rotation with respect to the projected tilt axis, and $\boldsymbol{\beta}$ is the offset angle between the 3-D tilt axis and the projection plane (Figure *14*a). There are five unknowns—$\boldsymbol{\alpha}, \boldsymbol{\beta}, (\boldsymbol{x_0^i}, \boldsymbol{y_0^i}, \boldsymbol{z_0^i})$ —in the above equation. At each tilt, two linearly independent equations can be provided—$(\boldsymbol{x^i(\theta)}, \boldsymbol{y^i(\theta)})$ are observables. Therefore, in principal, only three tilt images are needed to solve all the unknowns; in practice, however, a couple of tilt images are needed to average out drift and scan distortions.

The actual 3-D tilt-axis has a 1.5 degree take-off angle from the projection plane as evidenced by the $(\boldsymbol{x^i(\theta)}, \boldsymbol{y^i(\theta)})$ plot in Figure *14*b. Using the model based fitting method, particles positions and their rotational trajectory can be reconstructed (Figure *14*c).

This method can be further applied to a DNA-origami linked nanoassembly (Figure *15*). Using prior knowledge of the system—one gold nanoparticle in different sizes are supported on each vertex—a model based reconstruction of the assembly can be achieved (Figure *15*b). The model enables the geometrical analysis for designing objects with precise structural specifications.

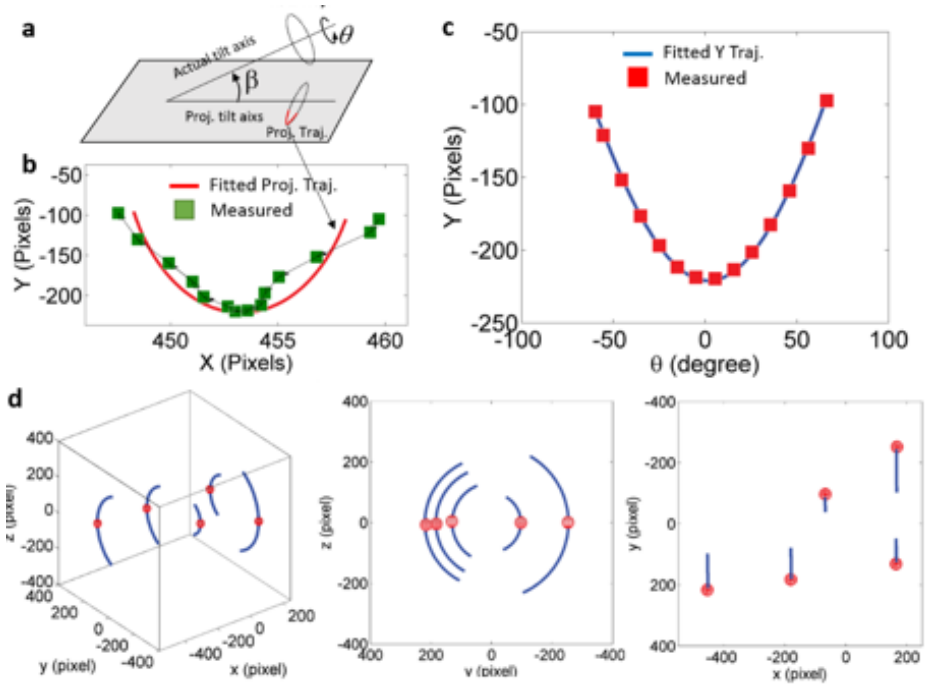

Figure 14 Model based fitting of the 3D particle position through Eq. (3-1). (a) A schematic plot showing the geometry of the actual tilt axis and the projected tilt axis. (b)Measured and modeled projected trajectory of a particle from -60 degrees to +60 degrees. The offset angle between then tilt axis and projection plane is determined to be 1.5 degrees. (c) The projected Y movement of the particle overlaid with the figged model. (d) Reconstructed 3-D position of five nanoparticles

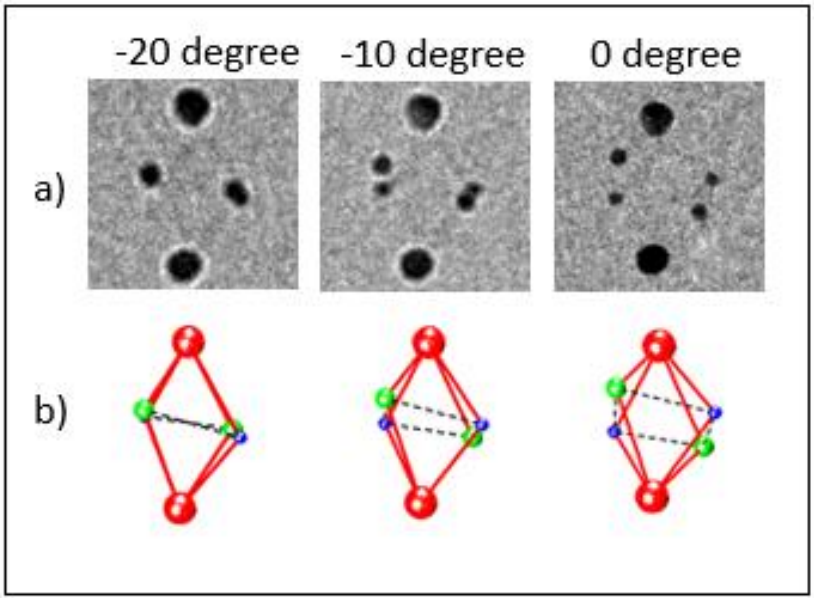

Figure 15 A model based reconstruction of DNA-origami linked nanoassmbly. (a) BF-TEM required at 200keV TEM (b) The reconstructed model of view at specified tilt angles.

Chapter 4 Conclusion

In this thesis, we covered most-used S/TEM characterization methods in both two dimension and three dimension. First of all, we investigated nanocatalysts: ternary alloy FePtNi NRs and Au/MnO NPs. Through several 2D characterization such as HR-TEM imaging, ADF-STEM imaging, STEM-EELS line scan and STEM-EELS 2D mapping, we found that: (1) NRs synthesised were structurally well-defined, ~26nm in length and ~5nm in wide. (2) The distribution of elements concentration indicated core-shell structure, in other words, iron and nickel were concentrated inside while platinum was rich outside. (3) 2D elemental mapping done on Au/Mn NPs which were insensitive to beam. An overlay image visualized distribution of gold and manganese. A core-shell structure with Au-rich inside was proved. After that we studied on electrode material (NiO nanosheet) for lithium-ion battery using in-situ TEM electrochemical test. From real-time tracking the morphology of NiO nanosheet, we observed two types of reaction, lateral and core-shell reaction, happened on the same material. From observation, we ensured that the reaction was a process of nucleation and prologation which was controlled by diffusion. The reason why huge difference in reaction time is expected for further study. We then focus on three dimensional characterization. We built a model based on tomograhic reconstruction which helped to shorten time to aquire tilting series. The model also accurated the reconstruction results since we found the take-off angle. This angle was about 1.5 degree between real axis and axis on projected plane. We then applied this model on DNA-origami linked nanoassemblies. Particle positions and their rotation trajectory were reconstruced using model based fitting method.

Reference

[1] Drexler, K. Eric (1986). *Engines of Creation: The Coming Era of Nanotechnology*. Doubleday.

[2] Williams, D and Carter, C. B. (1996). *Transmission Electron Microscopy*. 1 – Basics. Plenum Press. P69

[3] Williams, D and Carter, C. B. (1996). *Transmission Electron Microscopy*. 1 – Basics. Plenum Press. P74

[4] Williams, D and Carter, C. B. (1996). *Transmission Electron Microscopy*. 2 – Diffraction. Plenum Press. P179-183

[5] Williams, D and Carter, C. B. (1996). *Transmission Electron Microscopy*. 1 – Basics. Plenum Press. P144-146

[6] Ahn C C (ed.) (2004). *Transmission electron energy loss spectrometry in material science and the EELS Atlas*. Wiley, Weinheim.

[7]Midgley, P. A.; Ward, E. P. W.; Hungría, A. B.; Thomas, J. M. *Chemical Society Reviews* 2007, *36*, 1477.

[8] Williams, D and Carter, C. B. (1996). *Transmission Electron Microscopy*. 3 – Imaging. Plenum Press. P361-365

[9] Williams, D and Carter, C. B. (1996). *Transmission Electron Microscopy*. 1 – Basics. Plenum Press. P140

[10] Chapman, S.K (1980) *Understanding and optimizing Electron Microscope Performance 1.* *Transmission Microscopy*, Science Reviews Ltd.

[11] Williams, D and Carter, C. B. (1996). *Transmission Electron Microscopy*. 3 – Imaging. Plenum Press. P439-442

[12] Spence, John C. H. (1988) [1980]. *Experimental high-resolution electron microscopy*. New York: Oxford U.Press

[13] M. Varela, A. R. Lupini, K. van Benthem, A. Borisevich, M. F. Chisholm, N. Shibata,E. Abe, and S. J. Pennycook, in: Annu. Rev. Mater. Res., 35 (2005) 539–569

[14] Williams, D and Carter, C. B. (1996). *Transmission Electron Microscopy*. 2 – Diffraction. Plenum Press. P304

[15] Schwartz, L.H. and Cohen,J.B. (1977) *Diffraction from Materials*, Academic Press

[16] Andrews, K.W., D.J., and Keown, S.R. (1971) *Interpretation of Electron Diffraction Patterns*, 2nd edition, Plenum Press

[17] Williams, D and Carter, C. B. (1996). *Transmission Electron Microscopy*. 2 – Diffraction. Plenum Press. P306

[18] J.A. Eades, Appl (1986). Surf. Sci. **26**, 280

[19] Williams, D and Carter, C. B. (1996). *Transmission Electron Microscopy*. 2 – Diffraction. Plenum Press. P300-303

[20] S. J. Pennycook, A. R. Lupini, M. Varela, A. Borisevich, M. F. Chisholm, E. Abe, N. Dellby, O. L. Krivanek, P. D. Nellist, L. G. Wang, R. Buczko, X. Fan, and S. T. Pantelides, in: *Spatially Resolved Characterization of Local Phenomena in Materials and Nanostructures*, Vol. 738, D. A. Bonnell, A. J. Piqueras, P. Shreve, and F. Zypman (Eds.), Materials Research Society, Warrendale, Pennsylvania (2003), p. G1.1

[21] Russ, J.C. (1984) *Fundamentals of Energy Dispersive X-ray Analysis*, Butterworths, Boston, Massachusetts

[22] Egerton, R.F. (1996) *Electron Energy Loss Spectroscopy in Electron Microscope*, 2nd Edition, Plenum Press

[23] Williams, D and Carter, C. B. (1996). *Transmission Electron Microscopy*. 4 – Spectrometry. Plenum Press. P655-657

[24] Williams, D.B. (1987) *Practical Analytical Electron Microscopy in Material Science. 2nd Edition.* Phillips Electron Optics Publishing Group

[25] Russ, J.C. (1984) *Fundamentals of Energy Dispersive X-ray Analysis*, Butterworths, Boston, Massachusetts

[26] Midgley, P. A.; Ward, E. P. W.; Hungría, A. B.; Thomas, J. M. *Chemical Society Reviews* 2007, *36*, 1477.

[27] G.T. Herman, *Image Reconstruction from Projections, The fundamentals of Computerized Tomography*, Academic Press

[28] Richard I. Masel. (2001) *Chemical Kinetics and Catalysis*. Wiley-Interscience

[29] Pierluigi Barbaro, Francesca Liguori, ed. (2010). *Heterogenized homogeneous catalysts for fine chemicals production : materials and processes*. Dordrecht: Springer

[30] Chaturvedi, S.; Dave, P. N.; Shah, N. K. *Journal of Saudi Chemical Society* **2012**, *16*, 307-325.

[31] Wilsn, M.S., Gottesfeld, S., 1992. J. Appl. Electrochem. 1, 1.

[32] Oh, H.-S., Oh, J.-G., Hong, Y.-G., Kim, H. (2007) *Electrochem.* Acta 52, 7278.

[33] Zhu, H.; Zhang, S.; Guo, S.; Su, D.; Sun, S. *J Am Chem Soc* **2013**, *135*, 7130-7133.

[34] Hsieh, Yu-chi. et al. (2013) *Ordered bilayer ruthenium-platinum core-shell nanoparticles as carbon monoxide-tolerant fuel cell catalysts*. Nature communication

[35] Goodenough, J. B. and Y. Kim (2010). *Challenges for Rechargeable Li Batteries*. Chemistry of Materials 22(3): 587-603.

[36] Sides,C. R.; Li, N. C.; Patrissi, C. J.; Scrosati, B.; Martin, C. R. *Mrs Bull* **2002**, *27*, 604-607

[37] P.Poizot, S. Laruelle, S. Grugeon, L. Dupont, J-M. Tarascon, *Nano-sized transition-metal oxides as negative-electrode materials for lithium-ion batteries*,Nature(2000),407, 496-499

[38] Zhu, H.; Zhang, S.; Guo, S.; Su, D.; Sun, S. *J Am Chem Soc* **2013**, *135*, 7130-7133